HELDA
HELSINGIN YLIOPISTO
HELSINGFORS UNIVERSITET
UNIVERSITY OF HELSINKI

UNIVERSITY OF HELSINKI

https://helda.helsinki.fi

Tracking crystal-melt segregation and magma recharge using zircon trace element data

Yan, Li-Li

2020-06-05

Yan , L-L , He , Z-Y , Klemd , R , Beier , C & Xu , X-S 2020 , ' Tracking crystal-melt segregation and magma recharge using zircon trace element data ' , Chemical Geology , vol. 542 , 119596 . https://doi.org/10.1016/j.chemgeo.2020.119596

http://hdl.handle.net/10138/341992
https://doi.org/10.1016/j.chemgeo.2020.119596

cc_by_nc_nd
acceptedVersion

Downloaded from Helda, University of Helsinki institutional repository.

This is an electronic reprint of the original article.

This reprint may differ from the original in pagination and typographic detail.

Please cite the original version.

Journal Pre-proof

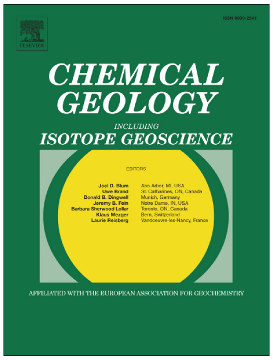

Tracking crystal-melt segregation and magma recharge using zircon trace element data

Li-Li Yan, Zhen-Yu He, Reiner Klemd, Christoph Beier, Xi-Sheng Xu

PII: S0009-2541(20)30135-2

DOI: https://doi.org/10.1016/j.chemgeo.2020.119596

Reference: CHEMGE 119596

To appear in: *Chemical Geology*

Received date: 28 September 2019

Revised date: 16 February 2020

Accepted date: 21 March 2020

Please cite this article as: L.-L. Yan, Z.-Y. He, R. Klemd, et al., Tracking crystal-melt segregation and magma recharge using zircon trace element data, *Chemical Geology* (2020), https://doi.org/10.1016/j.chemgeo.2020.119596

This is a PDF file of an article that has undergone enhancements after acceptance, such as the addition of a cover page and metadata, and formatting for readability, but it is not yet the definitive version of record. This version will undergo additional copyediting, typesetting and review before it is published in its final form, but we are providing this version to give early visibility of the article. Please note that, during the production process, errors may be discovered which could affect the content, and all legal disclaimers that apply to the journal pertain.

© 2020 Published by Elsevier.

Journal Pre-proof

Tracking crystal–melt segregation and magma recharge using zircon trace element data

Li-Li Yan[1], Zhen-Yu He[1,*], Reiner Klemd[2], Christoph Beier[3], Xi-Sheng Xu[4]

[1] *Key Laboratory of Deep-Earth Dynamics, Institute of Geology, Chinese Academy of Geological Sciences, Beijing 100037, China*

[2] *GeoZentrum Nordbayern, Friedrich-Alexander Universität Erlangen-Nürnberg (FAU), Schlossgarten 5, D-91054 Erlangen, Germany*

[3] *Department of Geosciences and Geography (GeoHel), University of Helsinki, PO Box 64, FIN-00014, Helsinki, Finland*

[4] *State Key Laboratory for Mineral Deposits Research, School of Earth Sciences and Engineering, Nanjing University, Nanjing, 210023, China*

* Corresponding author: Zhen-Yu He, Institute of Geology, CAGS, 26 Baiwanzhuang Road, Beijing 100037, China. Tel.: +86 10 68999735; fax: +86 10 68997803. E-mail address: ahhzy@163.com.

Submitted to: *Chemical Geology*

Revised version 2, 16 February, 2020

Journal Pre-proof

Journal Pre-proof

Abstract

The Cretaceous Yunshan caldera complex in SE China consists of an unusual coexisting assemblage of peraluminous and peralkaline rhyolites and a resurgent intra-caldera porphyritic quartz monzonite. In this study, we use zircon trace element data to study the compositional differences of zircons from cogenetic magmas and to track the evolution of the entire magmatic system. Our results indicate that the zircons from the peraluminous and peralkaline rhyolites formed from highly evolved compositions with high Hf concentrations and low Ti contents, and low Th/U and Zr/Hf ratios, which are distinct from those of the intrusive porphyritic quartz monzonite. Zircons from the peraluminous and peralkaline rhyolites display overlapping Zr/Hf and Hf, but the zircons from the peralkaline rhyolites have extremely low Eu/Eu* ratios (< 0.1) and Ti contents (2.26–13.3 ppm). The lack of overlapping zircon trace element compositions between the volcanic and intrusive caldera units is interpreted to represent crystal–melt segregation processes. In addition, zircon grains from the porphyritic quartz monzonite and a few zircon grains from the peraluminous rhyolite display distinctly bright rims and whole grains in cathodoluminescence imaging, which have high Ti, Zr/Hf, and Eu/Eu*, and are similar to those of zircons from the mafic microgranular enclave within the porphyritic quartz monzonite. We interpret these signatures to reflect crystallization from a relatively hot and less evolved magma indicating a magma chamber recharge event. We further developed a model in which the magmas of the peraluminous and peralkaline rhyolites were successively extracted from a primitive crystal mush by

Journal Pre-proof

crystal–melt segregation with a rejuvenation of the crystal mush after the extraction of the peraluminous rhyolitic melt, leaving behind residual mushes solidified as porphyritic quartz monzonite. Our study shows that trace element analyses of zircons can effectively be used to pinpoint multiple crystal–melt segregation and melt extraction events as well as magma recharge processes in silicic magmatic systems.

Keywords: Crystal–melt segregation; Magma differentiation; Magma recharge; SE China; Yunshan caldera complex

Journal Pre-proof

1. Introduction

In large silicic magmatic systems, rhyolitic magmas are thought to have been generated through crystal-melt segregation and melt extraction from a shallow intermediate-silicic crystal mush, which also is an effective mechanism controlling the chemical evolution of magmas from mafic to highly silicic compositions (Bachmann and Bergantz, 2004; Hildreth, 2004; Miller and Wark, 2008; Lipman and Bachmann, 2015; Bachmann and Huber, 2016). This process is consistent with geophysical observations that isolated pockets of crystal-poor eruptible magma occur in the shallow crust (Cooper and Kent, 2014; Floess et al., 2019). Zircon incorporates a variety of trace elements during the crystallization process, including rare-earth elements (REE), Hf, U, Th, and Ti but is relatively resistant to alteration and weathering over long geological timescales. The trace element composition of zircon has been used to reveal how magmas are stored and remobilized, and to identify differentiation processes during the various stages of magma evolution, because zircon occurs over a wide compositional range and its textural, trace element and isotopic composition is sensitive to the composition and temperature of the host melts (e.g., Claiborne et al., 2006, 2010; Gagnevin et al., 2010; Klemetti et al., 2011; Reid et al., 2011; Chamberlain et al., 2014; Kong et al., 2016; Deering et al., 2016; Buret et al., 2017; Bell et al., 2019; Zou et al., 2019).

Calderas often consist of a compositional continuum of volcanic rocks and intra-caldera subvolcanic plutons. They commonly show a close genetic connection although they may represent different stages of magmatic evolution and caldera-forming processes (de Silva and Gosnold, 2007; Lipman, 2007; Shane et al., 2012; Lipman and Bachmann, 2015). Caldera systems are ideally suited to improve our understanding of the complexities of magmatic processes because they retain a comprehensive temporal and compositional record of magma reservoir dynamics and multistage processes during magma evolution (e.g., Tappa et al., 2011; Barth et al., 2012; Deering et al., 2016; Yan et al., 2016; Wu et al., 2017). The Yunshan caldera complex in SE China consists of an unusual assemblage of coexisting high-silica peraluminous and peralkaline rhyolites, associated with an intra-caldera resurgent porphyritic quartz monzonite containing mafic microgranular enclaves (Fig. 1; Hong et al., 2013; Yan et al., 2018a; Chen et al., 2019). Previous studies have shown that different rocks from this volcanic–plutonic complex formed from the same primitive magma inferred from overlapping zircon U–Pb ages and Hf isotope compositions, and whole-rock Sr–Nd isotopic data (Yan et al., 2018a). However, tracing the

Journal Pre-proof

relationships between the two types of rhyolites and the magmatic process of the volcanic and plutonic rocks remains challenging.

Here, we present new zircon trace element data of volcanic and plutonic rocks from the Yunshan caldera complex analyzed by laser ablation–inductively coupled plasma–mass spectrometry (LA-ICP-MS). The comparison of zircon trace element data from different compositions from the Yunshan caldera provides important constraints on (1) the processes of crystal–melt segregation forming peraluminous and peralkaline rhyolitic melts, (2) the processes of magma recharge and rejuvenation, (3) the genetic relationship between the volcanic and associated intrusive rocks, and (4) the mechanisms that led to the formation of the highly evolved silicic magmas. We can show that trace element analyses of zircons reflect crystal–melt segregation and magma recharge processes of a single silicic magmatic system and highlight the role of multiple crystal–melt segregations in generating high-silica peralkaline rhyolites.

Journal Pre-proof

2. Geological background and petrography

The Yunshan caldera complex is situated in the Fujian Province of SE China, which is part of a larger, ca. 2000-km-long Cretaceous volcanic–plutonic complex belt in the coastal region of SE China. The volcanic rocks in this belt occur in several large volcanic fields intimately associated with shallow intra-caldera plutons. Magmatic activity occurred in an active continental margin environment associated with the westward subduction of the paleo-Pacific plate (Jahn, 1974; Zhou et al., 2006; He and Xu, 2012; Yan et al., 2016; Zhang et al., 2018; Chen et al., 2019).

The Yunshan caldera complex has an exposure of ~30 km^2, and is bordered by a ring-fault. The complex is composed of three volcanic units represented by three successive caldera-forming eruptions and an intra-caldera porphyritic quartz monzonite (Fig. 1; Hong et al., 2013; Yan et al., 2018a). The oldest volcanic unit consists of flow-banded and massive peraluminous rhyolite (Fig. 1) containing ~10–15 vol.% phenocrysts of alkali feldspar and plagioclase in a fine- to micro-grained holocrystalline matrix consisting of feldspar, quartz, and accessory biotite (Fig. 2a). Glomerocrysts of alkali feldspar, plagioclase, and Fe–Ti oxides are also present. Distinctive zones rich in spherulites and lithophysae developed on top of the unit. The second volcanic unit (Fig. 1) consists of pyroclastic flow deposits of welded lapilli tuff with obsidian blocks (Fig. 2b). The third and youngest volcanic unit that occurs in the central part of the caldera is dominated by flow-banded peralkaline rhyolite (Fig. 1), which has a micro-grained holocrystalline matrix with few phenocrysts (< 5 vol.%) of alkali feldspar, quartz, Na-rich amphibole (ferrorichterite and arfvedsonite), and minor clinopyroxene, magnetite, and ilmenite, but plagioclase phenocrysts are absent (Fig. 2c). A porphyritic quartz monzonite was emplaced into the center of the caldera along the conduit that was generated when previous rhyolites erupted (Fig. 1). The porphyritic quartz monzonite has ~40–50 vol.% phenocrysts dominated by alkali feldspar, plagioclase, quartz, amphibole (edenite to magnesiohornblende), and clinopyroxene. The fine-grained matrix mainly comprises alkali feldspar, plagioclase, quartz, and clinopyroxene with accessory biotite, magnetite, and apatite (Fig. 2d). Mafic microgranular enclaves (5–15 cm in diameter) sparsely occur in the host

Journal Pre-proof

porphyritic quartz monzonite, which contain plagioclase mantled by alkali feldspar, alkali feldspar, clinopyroxene, amphibole (magnesiohornblende and edenite), biotite, magnetite, ilmenite, quartz (in order of decreasing abundance), and accessory acicular apatite.

Both, the peraluminous rhyolite and peralkaline rhyolite are silica-rich with high SiO_2 contents (70.1–78.9 wt.%), while the porphyritic quartz monzonite has lower SiO_2 contents (61.8–63.2 wt.%). The peraluminous rhyolite has an alumina saturation index [A/CNK = molar $Al_2O_3/(CaO + Na_2O + K_2O)$] of 1.01–1.17 except for a few metaluminous compositions, while the peralkaline rhyolite has a high agpaitic index [NK/A = molar $(Na_2O + K_2O)/Al_2O_3$] of 0.96–1.04 (Fig. 3).

SHRIMP zircon U–Pb geochronology of the Yunshan caldera complex revealed indistinguishable ages between 95.6 and 93.6 Ma (Fig. 4a; Yan et al., 2018a) within analytical uncertainties of the technique (Li et al., 2015). In addition, SHRIMP U–Pb dating results of individual samples show a large scatter of zircon ages, perhaps reflecting a protracted zircon crystallization in upper-crustal magma reservoirs (Samperton et al., 2015). The geochronological and geochemical data, and structural evidence support a genetic link between the Yunshan volcanic units and the intra-caldera intrusions (e.g., Deering et al., 2016; Buret et al., 2017).

3. Analytical methods

Zircon grains from two peraluminous rhyolite samples (F379-1 and F380-1), two peralkaline rhyolite samples (F374-1 and F376-1), one porphyritic quartz monzonite

Journal Pre-proof

(F371-2) and one mafic microgranular enclave (F371-1) samples (Fig. 1) were analyzed for their trace element compositions. Cathodoluminescence (CL) images of the analyzed zircon grains were obtained using an FEI NOVA NanoSEM 450 scanning electron microscope equipped with a Gatan Mono CL4 cathodoluminescence system at the Institute of Geology, Chinese Academy of Geological Sciences. Analytical sites were checked under transmitted light images in order to ensure that they were free of visible inclusions and fractures.

The zircon trace elements were analyzed at the GeoZentrum Nordbayern, Friedrich-Alexander Universität Erlangen-Nürnberg (FAU), Germany, using a 193 nm Analyte Excite laser ablation system (Teledyne Photon Machines) connected to an Agilent 7500c quadrupole ICP-MS (Plasma power 1100 W). The laser was operated using a spot size of 20–35 μm, a frequency of 20 Hz and a beam fluence of 3.0 J/cm^2. The acquisition time for each analysis was 43 s including 20 s for background scanning. Integration times were 10 ms for ^{29}Si, 30 ms for ^{31}P, ^{49}Ti, ^{51}V, ^{53}Cr, ^{88}Sr, ^{89}Y, ^{93}Nb, ^{117}Sn, ^{137}Ba, ^{139}La, ^{140}Ce, ^{141}Pr, ^{146}Nd, ^{147}Sm, ^{153}Eu, ^{157}Gd, ^{177}Hf, ^{178}Hf, ^{181}Ta, ^{232}Th, and ^{238}U, and 25 ms for ^{159}Tb, ^{163}Dy, ^{165}Ho, ^{166}Er, ^{169}Tm, ^{172}Yb, and ^{175}Lu. We used mass ^{49}Ti to calculate Ti concentrations to avoid the overlapping interferences from Zr (Szymanowski et al., 2018). Calibration was performed using NIST standard glass 612 (Pearce et al., 1997) with ^{29}Si as the internal standard. USGS basalt glass BCR-2G (Jacob, 2006) was analyzed as quality control reference material. The accuracy of the measurements was also checked using the 91500 zircon standard (Coble et al., 2018). Analyses of the standards and the calculated analytical precision

Journal Pre-proof

and accuracy are provided in Supplementary Table 1. The estimated accuracy of trace element analysis in this study is commonly less than 10% error except for Ti (with 14.4% error). The raw ICP-MS data were processed using GLITTER version 4.4.4, On-line Interactive Data Reduction for LA-ICPMS (Van Achterbergh et al., 2001). We convert Hf abundance into Zr/Hf ratios using a stoichiometric Zr content of 500,000 ppm. The measured zircon trace element compositions and 1 sigma errors are provided in Supplementary Table 2.

4. Results

The zircon grains from the six studied samples show characteristic morphologies and internal structures in the CL images (Fig. 5). Zircon grains from the peraluminous and peralkaline rhyolite samples are euhedral with oscillatory growth zoning. The zircon grains from the peraluminous rhyolite tend to be brighter and display a weaker zoning than those in the peralkaline rhyolite (Fig. 5a-d). A few zircon grains from the peraluminous rhyolite display relatively CL-bright rims. Zircon grains from the porphyritic quartz monzonite sample are characterized by oscillatory zoned dark cores, surrounded by weakly zoned or unzoned bright rims with resorption boundaries (Fig. 5e). The CL-bright zircon domains also occur as individual whole crystals. Zircon grains from the mafic microgranular enclave are unzoned or display a banded zoning (Fig. 5f).

Zircons from the peraluminous rhyolite, peralkaline rhyolite, porphyritic quartz monzonite, and mafic microgranular enclave have distinctly different trace element

Journal Pre-proof

compositions (Fig. 6; Supplementary Table 2). Zircons from the peraluminous rhyolite and the peralkaline rhyolite contain similarly lower Ti (2.26–32.3 ppm) contents, Th/U (0.44–1.47), and Zr/Hf (45–61) ratios, and higher Hf (8,152–11,017 ppm) contents and Yb/Gd (8.8–15.5) ratios compared to zircons from the porphyritic quartz monzonite and mafic microgranular enclave samples [cf. Ti (13.4–67.5 ppm), Th/U (0.84–2.58), and Zr/Hf (54–77), and Hf (6,472–9,258 ppm) and Yb/Gd (7.1–13.3)] (Fig. 6). However, zircon trace elements of the peralkaline rhyolite are distinct from those of the peraluminous rhyolite in having lower Eu/Eu* [$Eu/Eu^* = Eu_N/(Sm_N \times Gd_N)^{0.5}$] (0.02–0.05), Th/U (0.44–0.98), and Ti (2.26–13.3 ppm). The Eu/Eu* ratios of zircons from the peraluminous rhyolite (0.12–0.51) are close to those of the porphyritic quartz monzonite (0.04–0.69) (Fig. 6).

5. Discussion

5.1. Crystal–melt segregation and magma differentiation revealed by zircon trace elements

Igneous zircon is useful in tracking the magma evolution process of its host rock, because it grows over a wide range of mafic to silicic compositions. The trace elements in zircon solid solutions can reflect geochemical features of their parent magmas and the magmatic process fractionating the trace elements. Hafnium concentrations and Zr/Hf ratios of zircon are conventional monitors of the evolution of parent melt where high Hf concentrations and low Zr/Hf ratios in zircon corresponds to mineral growth in a relatively evolved melt (Claiborne et al., 2006;

Journal Pre-proof

Deering et al., 2016; Wu et al., 2017). In addition, zircon crystallization with decreasing temperature of the melt can be assessed where decreasing Ti contents are accompanied by increasing Hf concentrations (Watson and Harrison, 2005; Watson et al., 2006; Ferry and Watson, 2007).

Zircons from the peraluminous and peralkaline rhyolites and the intra-caldera plutons of the Yunshan caldera complex generally straddle amongst two distinct groups in Hf and Ti concentrations, and Zr/Hf, Th/U, and Yb/Gd ratios (Fig. 6). The rhyolite zircons display a highly evolved signature with relatively high Hf but low Ti contents and Zr/Hf ratios (Fig. 6). In contrast, zircons from the porphyritic quartz monzonite have relatively high Ti contents, and low Hf concentrations and Zr/Hf ratios, implying that they formed from a less-evolved melt (Fig. 6; Claiborne et al., 2006, 2010; Barth et al., 2013; Klemetti and Clynne, 2014; Deering et al., 2016; Schaen et al., 2017).

Zircon grains from the peraluminous rhyolite, peralkaline rhyolite, and porphyritic quartz monzonite have consistent U–Pb ages, and Hf isotope compositions, suggesting that the zircons crystallized from melts, which were derived from the same primitive magma (Fig. 4; Yan et al., 2018a). This observation is consistent with the petrogenetic link between volcanic and plutonic rocks from the same caldera, suggesting that the magmas of the volcanic lithologies were extracted from a silicic crystal mush (Bachmann et al., 2007; de Silva and Gosnold, 2007; Lipman, 2007; Miller and Wark, 2008) crystallizing zircons with evolved trace-element compositions, whereas the plutonic rocks formed from solidified residual mushes, corresponding to

Journal Pre-proof

lower degrees of fractionation (Deering et al., 2016; Schaen et al., 2017; Yan et al., 2018b). This interpretation is also supported by the whole-rock compositions in which the porphyritic quartz monzonite has an intermediate composition (SiO_2 = 62–63 wt.%), separated by a Daly Gap (63–70 wt.%) from the peraluminous and peralkaline rhyolites, and a Eu/Eu* close to unity and relatively high Sr and low Rb concentrations reflecting feldspar accumulation (Fig. 7).

It has been suggested that zircon grains may continuously be mobilized in extracting melts but may also remain in the crystal mushes during crystal–melt segregation events (Deering et al., 2016; Buret et al., 2017; Schaen et al., 2017; Yan et al., 2018b). Here, we observe a minor overlap between the zircon trace element contents of the peraluminous rhyolite and those from the porphyritic quartz monzonite, with respect to their Eu/Eu*, Yb/Gd, and Zr/Hf ratios, and Ti contents (Fig. 6). We propose that a few zircon grains from the peraluminous rhyolite may be captured from the crystal mush indicating a prolonged contact between the rhyolitic melt and crystal mush, similar to the cases of Deering et al. (2016) and Yan et al. (2018b) (see a comparison in Fig. 6). However we note that most zircon grains (with distinctively low Zr/Hf) crystallized directly from the host peraluminous rhyolitic magma concordant with the crystal–melt segregation processes.

In order to verify our observations, we modeled the crystal–melt segregation processes for the formation of the peraluminous rhyolite using a Rayleigh fractional crystallization model (model 1; Fig. 6d). The distinct Zr/Hf ratios of the zircons from the peraluminous rhyolite and the porphyritic quartz monzonite indicate zircon

Journal Pre-proof

crystallization and accumulation in a zircon-saturated mush. The comparable Eu/Eu* ratios of the peraluminous rhyolite and the porphyritic quartz monzonite indicate little plagioclase fractionation. The high A/CNK ratios of the peraluminous rhyolite (Fig. 3) indicate crystal fractionation of amphibole and/or pyroxene due to their relatively low A/CNK ratios (< 1.0) (Wu et al., 2017). Our modeling results show that the peraluminous rhyolite can be produced by 50% fractional crystallization of K-feldspar (35%), plagioclase (30%), amphibole (20%), clinopyroxene (10%), biotite (5%), and accessory zircon (0.01%) from the starting melt composition calculated from the most primitive zircon composition (F371-1-15) of the mafic microgranular enclave (Fig. 6d).

The solubility of zircon in peralkaline melts is much higher than that in peraluminous and metaluminous melts and once a melt has reached zircon-saturation this process is non-reversable (Watson, 1979; Miller et al., 2003). This is consistent with similar Zr/Hf ratios and Hf concentrations of zircons from the peraluminous and peralkaline rhyolites, indicating that the peralkaline melt was extracted from a zircon-undersaturated mush without growth of zircon. Therefore, we suggest that rejuvenation of the crystal mush through the injection of a more primitive magma occurred after extraction of peraluminous rhyolitic melt in a cooling magmatic system. Magma rejuvenation is also evidenced by the occurrence of partial dissolution features and resorbed core regions of zircon from the peraluminous rhyolite (Fig. 5; Miller and Wooden, 2004; Claiborne et al., 2010). The consistently low Eu/Eu* ratios (< 0.1) of zircons from the peralkaline rhyolite reflects that the magma experienced

Journal Pre-proof

plagioclase-dominated fractionation before the extraction of the peralkaline rhyolitic melt (Fig. 6; Reid et al., 2011; Trail et al., 2012). In addition, the low Ti contents and Th/U ratios of the peralkaline rhyolite zircons indicate that they formed from a more evolved melt resulting in the eruption of the peralkaline rhyolite, supported by the evolved whole-rock characteristics (lowest Sr and Eu/Eu*; Fig. 7). Our Rayleigh fractional crystallization model for the peralkaline rhyolite melt is based on a starting composition derived from a mixed composition of the peraluminous rhyolite and the mafic microgranular enclave (model 2). The modeling results show that the peralkaline rhyolites can be produced by 70% fractional crystallization of K-feldspar (15%) + plagioclase (55%) + clinopyroxene (15%) + magnetite (10%) + amphibole (5%; Fig. 6d).

Considering the spatial and temporal relationship of the peraluminous and peralkaline rhyolites, we suggest a model in which the magmas that formed the peraluminous and peralkaline rhyolites were different batches of melt extracted from silicic crystal mushes. The peraluminous rhyolitic melts were initially extracted from a silicic mush (Fig. 8a). The silicic mush was rejuvenated by a mafic magma recharge event after the extraction of peraluminous rhyolitic melt and then underwent plagioclase dominated fractionation, which ultimately resulted in a peralkaline composition of the extracted melt (Fig. 8b). The zircon grains from both the peraluminous and peralkaline rhyolites mainly crystallized from their respective host magmas, indicating a crystal–melt segregation process. In addition, the extracted peraluminous and peralkaline rhyolitic magmas were continuously assembled and

Journal Pre-proof

stored in a melt lens within the mush zone prior to eruption (Fig. 8), concordant with a protracted duration of zircon crystallization revealed by SHRIMP U–Pb dating results (Fig. 4a).

5.2. Magma recharge events revealed by multistage crystallization of zircon from the porphyritic quartz monzonite

The occurrence of distinct zircon trace element domains or crystals from the porphyritic quartz monzonite and from the peraluminous rhyolite reflects changes in melt composition during zircon crystallization (Claiborne et al., 2010; Reid et al., 2011; Chamberlain et al., 2014; Large et al., 2018; Yan et al., 2018b). The zircon cores are partly resorbed and have dissolution features (Fig. 5). The CL-bright zircon rims or crystals show comparatively lower Hf, Th, and U, and higher Ti contents, as well as higher Zr/Hf and Eu/Eu* ratios compared to the zircon cores (Fig. 6). Their high Ti and low Hf contents are consistent with high crystallization temperatures (Fig. 6a; Watson and Harrison, 2005; Watson et al., 2006; Ferry and Watson, 2007). This texture and composition change is thus best explained by the involvement of a hot and less evolved melt and likely records a magma recharge process (Ferry and Watson, 2007; Claiborne et al., 2010; Chamberlain et al., 2014; Klemetti and Clynne, 2014; Large et al., 2018). The boundaries between zircon core and rim domains have typical resorption textures (Fig. 5e), indicating dissolution and overgrowth of zircon in the presence of a hot melt (e.g., Bachmann et al., 2002; Wark et al., 2007; Wolff et al., 2015; Watts et al., 2016). The occurrence of mafic microgranular enclaves in the

Journal Pre-proof

porphyritic quartz monzonite also provides petrographic evidence for the occurrence of a hot and less evolved recharge magma (e.g., Bachmann et al., 2002; Wright et al., 2011; Kennedy et al., 2016; Buret et al., 2017).

In addition, zircons from the mafic microgranular enclave and CL-bright zircons from the porphyritic quartz monzonite have comparable trace element compositions, i.e., high Zr/Hf and Eu/Eu* ratios, as well as high Ti contents (Figs. 5 and 6), suggesting that both crystallized from the recharge magma. Some overlapping zircon trace element compositions between zircons from the mafic microgranular enclave and zircon cores from the porphyritic quartz monzonite may be related to small-scale magma mixing between the magma in the reservoir and the recharge magma. This supports magma recharging and rejuvenation of a crystal mush beneath the Yunshan caldera complex (Fig. 8). The recharge magma may lead to thermal reactivation of a rheologically locked crystal mush and may also promote the crystal-melt segregation, rhyolitic melt extraction and the rhyolite eruption as well as emplacement of the resurgent intra-caldera intrusions (e.g., Charlier et al., 2007; Wright et al., 2011; Pistone et al., 2015; Sliwinski et al., 2017; Floess et al., 2019; Sun et al., 2019).

Journal Pre-proof

6. Conclusions

(1) The distinct zircon trace element signatures of the coeval volcanic and plutonic rocks from the Yunshan caldera complex reveal that the magmas that formed the peraluminous and peralkaline rhyolites were successively extracted from silicic crystal mushes via crystal–melt segregation. Followed by an interval of

rejuvenation of the crystal mush after the extraction of peraluminous rhyolitic melt, the residual mushes solidified as porphyritic quartz monzonite. This indicates that the magma differentiation via melt extraction from crystal mushes is an effective mechanism for generating high-silica rhyolite melts.

(2) Zircons from the resurgent intra-caldera porphyritic quartz monzonite were subdivided into two types due to their different CL- and chemical zoning characteristics, indicating the rejuvenation of the crystal mush by hotter and less-evolved recharge magmas. The rejuvenation is also responsible for changing the compositions of extracted melts from peraluminous to peralkaline.

(3) Our study shows that trace element analyses of zircons from coeval plutonic and volcanic rocks can effectively be used to elucidate magmatic processes such as multiple crystal–melt segregation and melt extraction events as well as magma recharge processes in silicic magmatic systems.

Journal Pre-proof

Acknowledgments

We thank Russell Bailie, Donald Dingwell, E. B. Watson, and two anonymous reviewers for their helpful and constructive reviews. We are grateful to H. Brätz for assistance with the LA-ICP-MS analysis. This work was supported by the National Natural Science Foundation of China (grant numbers 41930214, 41102028). ChB is grateful to W. Bach and P. Charlotte of being able to work on the manuscript during expedition MSM86. This publication is a contribution to the IGCP Project 662.

Journal Pre-proof

References

Bachmann, O., Dungan, M.A., Lipman, P.W., 2002. The Fish Canyon magma body, San Juan volcanic field, Colorado: rejuvenation and eruption of an upper-crustal batholith. J. Petrol. 43, 1469–1503.

Bachmann, O., Bergantz, G.W., 2004. On the origin of crystal-poor rhyolites: extracted from batholithic crystal mushes. J. Petrol. 45, 1565–1582.

Bachmann, O., Miller, C.F., de Silva, S.L., 2007. The volcanic–plutonic connection as a stage for understanding crustal magmatism. J. Volcanol. Geotherm. Res. 167, 1–23.

Bachmann, O., Huber, C., 2016. Silicic magma reservoirs in the Earth’s crust. Am. Mineral. 101, 2377–2404.

Barth, A., Feilen, A., Yager, S., Douglas, S., Wooden, J., Riggs, N., Walker, J., 2012. Petrogenetic connections between ash-flow tuffs and a granodioritic to granitic intrusive suite in the Sierra Nevada arc, California. Geosphere 8, 250–264.

Barth, A.P., Wooden, J.L., Jacobson, C.E., Economos, R.C., 2013. Detrital zircon as a proxy for tracking the magmatic arc system: the California arc example. Geology 41, 223–226.

Bell, E.A., Boehnke, P., Barboni, M., Harrison, T.M., 2019. Tracking chemical alteration in magmatic zircon using rare earth element abundances. Chem. Geol. 510, 56–71.

Buret, Y., Wotzlaw, J., Roozen, S., Guillong, M., Von Quadt, A., Heinrich, C.A., 2017. Zircon petrochronological evidence for a plutonic-volcanic connection in porphyry copper deposits. Geology 45, 623–626.

Chamberlain, K.J., Wilson, C.J., Wooden, J.L., Charlier, B.L., Ireland, T.R., 2014. New perspectives on the Bishop Tuff from zircon textures, ages and trace elements. J. Petrol. 55, 395–426.

Charlier, B.L.A., Bachmann, O., Davidson, J.P., Dungan, M.A., Morgan, D.J., 2007. The upper crustal evolution of a large silicic magma body: evidence from crystal-scale Rb–Sr isotopic heterogeneities in the Fish Canyon magmatic system, Colorado. J. Petrol. 48, 1875–1894.

Chen, J.-Y., Yang, J.-H., Zhang, J.-H., 2019. Origin of Cretaceous aluminous and peralkaline A-type granitoids in northeastern Fujian, coastal region of southeastern China. Lithos 340-341, 223–238.

Claiborne, L.L., Miller, C., Walker, B., Wooden, J., Mazdab, F., Bea, F., 2006. Tracking magmatic processes through Zr/Hf ratios in rocks and Hf and Ti zoning in zircons: an example from the Spirit Mountain batholith, Nevada. Mineral. Mag. 70, 517–543.

Claiborne, L.L., Miller, C.F., Wooden J.L., 2010. Trace element composition of igneous zircon: a thermal and compositional record of the accumulation and evolution of a large silicic batholith, Spirit Mountain, Nevada. Contrib. Mineral. Petrol. 160, 511–531.

Coble, M.A., Vazquez, J.A., Barth, A.P., Wooden, J.L., Burns, D.H., Kylanderclark, A.R.C., Jackson, S.E., Vennari, C.E., 2018. Trace Element Characterisation of MAD-559 Zircon Reference Material for Ion Microprobe Analysis. Geostand.

Journal Pre-proof

Journal Pre-proof

Geoanal. Res. 42, 481–497.

Cooper, K.M., Kent, A.J.R., 2014. Rapid remobilization of magmatic crystals kept in cold storage. Nature 506, 480–483.

de Silva, S.L., Gosnold, W.D., 2007. Episodic construction of batholiths: insights from the spatiotemporal development of an ignimbrite flare-up. J. Volcanol. Geotherm. Res. 167, 320–335.

Deering, C.D., Keller, B., Schoene, B., Bachmann, O., Beane, R., Ovtcharova, M., 2016. Zircon record of the plutonic-volcanic connection and protracted rhyolite melt evolution. Geology 44, 267–270.

Ferry, J.M., Watson, E.B., 2007. New thermodynamic models and revised calibrations for the Ti-in-zircon and Zr-in-rutile thermometers. Contrib. Mineral. Petrol. 154, 429–437.

Floess, D., Caricchi, L., Simpson, G., Wallis, S.R., 2019. Melt segregation and the architecture of magmatic reservoirs: insights from the Muroto sill (Japan). Contrib. Mineral. Petrol. 174, 27.

Gagnevin, D., Daly, J.S., Kronz, A., 2010. Zircon texture and chemical composition as a guide to magmatic processes and mixing in a granitic environment and coeval volcanic system. Contrib. Mineral. Petrol. 159, 579–596.

He, Z.Y., Xu, X.S., 2012. Petrogenesis of the Late Yanshanian mantle-derived intrusions in southeastern China: response to the geodynamics of paleo-Pacific plate subduction. Chem. Geol. 328, 208–221.

Hildreth, W., 2004. Volcanological perspectives on Long Valley, Mammoth Mountain, and Mono Craters: several contiguous but discrete systems. J. Volcanol. Geotherm. Res. 136, 169–198.

Hong, W.T., Xu, X.S., Zou, H.B., 2013. Petrogenesis of coexisting high–silica aluminous and peralkaline rhyolites from Yunshan (Yongtai), southeastern China. J. Asian Earth Sci. 74, 316–329.

Jacob, D., 2006. High sensitivity analysis of trace element-poor geological reference glasses by laser ablation–inductively coupled plasma-mass spectrometry (LA-ICP-MS). Geostand. Geoanal. Res. 30, 221–235.

Jahn, B.-m., 1974. Mesozoic thermal events in southeast China. Nature 248, 480.

Kennedy, B., Stix, J., Hon, K., Deering, C., Gelman, S., 2016. Magma storage, differentiation, and interaction at Lake City caldera, Colorado, USA. Geol. Soc. Am. Bull. 128, 764–776.

Klemetti, E.W., Deering, C.D., Cooper, K.M., Roeske, S.M., 2011. Magmatic perturbations in the Okataina Volcanic Complex, New Zealand at thousand-year timescales recorded in single zircon crystals. Earth Planet. Sci. Lett. 305, 185–194.

Klemetti, E.W., Clynne, M.A., 2014. Localized rejuvenation of a crystal mush recorded in zircon temporal and compositional variation at the Lassen Volcanic Center, northern California. PLoS ONE 9, e113157.

Kong, D.-X., Xu, J.-F., Chen, J.-L., 2016. Oxygen isotope and trace element geochemistry of zircons from porphyry copper system: implications for Late Triassic metallogenesis within the Yidun Terrane, southeastern Tibetan Plateau.

Journal Pre-proof

Chem. Geol. 441, 148–161.

Large, S.J., Quadt, A.v., Wotzlaw, J.F., Guillong, M., Heinrich, C.A., 2018. Magma evolution leading to porphyry Au–Cu mineralization at the Ok Tedi deposit, Papua New Guinea: trace element geochemistry and high-precision geochronology of igneous zircon. Econ. Geol. 113, 39–61.

Li, X., Liu, X., Liu, Y., Su, L., Sun, W., Huang, H., Yi, K., 2015. Accuracy of LA-ICPMS zircon U–Pb age determination: an inter-laboratory comparison. Sci. Chin. Earth Sci. 58, 1722–1730.

Lipman, P.W., 2007. Incremental assembly and prolonged consolidation of Cordilleran magma chambers: evidence from the Southern Rocky Mountain volcanic field. Geosphere 3, 42–70.

Lipman, P.W., Bachmann, O., 2015. Ignimbrites to batholiths: integrating perspectives from geological, geophysical, and geochronological data. Geosphere 11, 705–743.

Ludwig, K.R., 2001. User's Manual for Isoplot/Ex (Rev.2.49): A geochronological toolkit for Microsoft Excel. Berkeley Geochronology Center, Special Publication 1a 55.

Maniar, P.D., Piccoli, P.M., 1989. Tectonic discrimination of granitoids. Geol. Soc. Am. Bull. 101, 635–643.

Miller, C.F., McDowell, S.M., Mapes, R.W., 2003. Hot and cold granites? Implications of zircon saturation and preservation of inheritance. Geology 31, 529–532.

Journal Pre-proof

Miller, J.S., Wooden, J.L., 2004. Residence, resorption and recycling of zircons in Devils Kitchen rhyolite, Coso Volcanic Field, California. J. Petrol. 45, 2155–2170.

Miller, C.F., Wark, D.A., 2008. Supervolcanoes and their explosive supereruptions. Elements 4, 11–15.

Pearce, N.J.G., Perkins, W.T., Westgate, J.A., Gorton, M.P., Jackson, S.E., Neal, C.R., Chenery, S.P., 1997. A compilation of new and published major and trace element data for NIST SRM 610 and NIST SRM 612 glass reference materials. Geostand. Newslett. 21, 115–144.

Pistone, M., Arzilli, F., Dobson, K.J., Cordonnier, B., Reusser, E., Ulmer, P., Marone, F., Whittington, A.G., Mancini, L., Fife, J., 2015. Gas-driven filter pressing in magmas: insights into in-situ melt segregation from crystal mushes. Geology 43, 699–702.

Reid, M.R., Vazquez, J.A., Schmitt, A.K., 2011. Zircon-scale insights into the history of a supervolcano, Bishop Tuff, Long Valley, California, with implications for the Ti-in-zircon geothermometer. Contrib. Mineral. Petrol. 161, 293–311.

Samperton, K.M., Schoene, B., Cottle, J.M., Keller, C.B., Crowley, J.L., Schmitz, M.D., 2015. Magma emplacement, differentiation and cooling in the middle crust: integrated zircon geochronological–geochemical constraints from the Bergell Intrusion, Central Alps. Chem. Geol. 417, 322–340.

Schaen, A.J., Cottle, J.M., Singer, B.S., Keller, C.B., Garibaldi, N., 2017. Complementary crystal accumulation and rhyolite melt segregation in a late

Journal Pre-proof

Miocene Andean pluton. Geology 45, 835–838.

Shane, P., Storm, S., Schmitt, A.K., Lindsay, J.M., 2012. Timing and conditions of formation of granitoid clasts erupted in recent pyroclastic deposits from Tarawera Volcano (New Zealand). Lithos 140-141, 1–10.

Sliwinski, J.T., Bachmann, O., Dungan, M.A., Huber, C., Deering, C.D., Lipman, P.W., Martin, L.H.J., Liebske, C., 2017. Rapid pre-eruptive thermal rejuvenation in a large silicic magma body: the case of the Masonic Park Tuff, Southern Rocky Mountain volcanic field, CO, USA. Contrib. Mineral. Petrol. 172, 30.

Sun, J.-F., Zhang, J.-H., Yang, J.-H., Yang, Y.-H., Chen, S., 2019. Tracing magma mixing and crystal–melt segregation in the genesis of syenite with mafic enclaves: evidence from in situ zircon Hf–O and apatite Sr–Nd isotopes. Lithos 334-335, 42–57.

Szymanowski, D., Fehr, M.A., Guillong, M., Coble, M.A., Wotzlaw, J.-F., Nasdala, L., Ellis, B.S., Bachmann, O., Schönbächler, M., 2018. Isotope-dilution anchoring of zircon reference materials for accurate Ti-in-zircon thermometry. Chem. Geol. 481, 146–154.

Tappa, M.J., Coleman, D.S., Mills, R.D., Samperton, K.M., 2011. The plutonic record of a silicic ignimbrite from the Latir volcanic field, New Mexico. Geochem. Geophys. Geosyst. 12, 1–16.

Trail, D., Watson, E.B., Tailby, N.D., 2012. Ce and Eu anomalies in zircon as proxies for the oxidation state of magmas. Geochim. Cosmochim. Acta 97, 70–87.

Van Achterbergh, E., Ryan, C.G., Jackson, S.E., Griffin, W.L., 2001. Data reduction

Journal Pre-proof

software for LA-ICP-MS: appendix. In: Sylvester, P.J. (Ed.), Laser Ablation-ICP-Mass Spectrometry in the Earth Sciences: Principles and Applications, Mineralog. Assoc. Canada (MAC) Short Course Series, Ottawa, Ontario, Canada, 29, pp. 239–243.

Wark, D.A., Hildreth, W., Spear, F.S., Cherniak, D.J., Watson, E.B., 2007. Pre-eruption recharge of the Bishop magma system. Geology 35, 235–238.

Watson, E.B., 1979. Zircon saturation in felsic liquids: experimental results and applications to trace element geochemistry. Contrib. Mineral. Petrol. 70, 407–419.

Watson, E.B., Harrison, T.M., 2005. Zircon thermometer reveals minimum melting conditions on earliest Earth. Science 308, 841–844.

Watson, E.B., Wark, D.A., Thomas, J.B., 2006. Crystallization thermometers for zircon and rutile. Contrib. Mineral. Petrol. 151, 413–433.

Watts, K.E., John, D.A., Colgan, J.P., Henry, C.D., Bindeman, I.N., Schmitt, A.K., 2016. Probing the volcanic–plutonic connection and the genesis of crystal-rich rhyolite in a deeply dissected supervolcano in the Nevada Great Basin: source of the late Eocene Caetano Tuff. J. Petrol. 57, 1599–1644.

Wolff, J.A., Ellis, B.S., Ramos, F.C., Starkel, W.A., Boroughs, S., Olin, P.H., Bachmann, O., 2015. Remelting of cumulates as a process for producing chemical zoning in silicic tuffs: a comparison of cool, wet and hot, dry rhyolitic magma systems. Lithos 236, 275–286.

Wright, H.M., Folkes, C.B., Cas, R.A., Cashman, K.V., 2011. Heterogeneous pumice

Journal Pre-proof

populations in the 2.08-Ma Cerro Galán Ignimbrite: implications for magma recharge and ascent preceding a large-volume silicic eruption. Bull. Volcanol. 73, 1513–1533.

Wu, F., Liu, X., Ji, W., Wang, J., Yang, L., 2017. Highly fractionated granites: recognition and research. Sci. Chin. Earth Sci. 60, 1201–1219.

Yan, L.-L., He, Z.-Y., Jahn, B.-m., Zhao, Z.-D., 2016. Formation of the Yandangshan volcanic–plutonic complex (SE China) by melt extraction and crystal accumulation. Lithos 266, 287–308.

Yan, L., He, Z., Beier, C., Klemd, R., 2018a. Geochemical constraints on the link between volcanism and plutonism at the Yunshan caldera complex, SE China. Contrib. Mineral. Petrol. 173, 4.

Yan, L.-L., He, Z.-Y., Beier, C., Klemd, R., 2018b. Zircon trace element constrains on the link between volcanism and plutonism in SE China. Lithos 320, 28–34.

Zhang, J.-H., Yang, J.-H., Chen, J.-Y., Wu, F.-Y., Wilde, S.A., 2018. Genesis of late Early Cretaceous high-silica rhyolites in eastern Zhejiang Province, southeast China: a crystal mush origin with mantle input. Lithos 296-299, 482–495.

Zhou, X.M., Sun, T., Shen, W.Z., Shu, L.S., Niu, Y.L., 2006. Petrogenesis of Mesozoic granitoids and volcanic rocks in South China: a response to tectonic evolution. Episodes 29, 26–33.

Zou, X., Qin, K., Han, X., Li, G., Evans, N.J., Li, Z., Yang, W., 2019. Insight into zircon REE oxy-barometers: a lattice strain model perspective. Earth Planet. Sci. Lett. 506, 87–96.

Journal Pre-proof

Figure Captions

Fig. 1. Geological sketch map of the Yunshan caldera complex, SE China, showing the distribution of the volcanic and intra-caldera plutonic rocks, and sample localities (modified from Yan et al., 2018a).

Fig. 2. Photomicrographs of volcanic and plutonic rocks from the Yunshan caldera complex (a and d in crossed nicols; b and c in parallel nicols). (a) Peraluminous rhyolite from the oldest volcanic unit showing the alkali feldspar and plagioclase phenocrysts in a fine- to micro-grained holocrystalline matrix. (b) Obsidian from the second volcanic unit. (c) Peralkaline rhyolite from the youngest volcanic unit showing alkali feldspar, quartz, and ferrorichterite phenocrysts. (d) Porphyritic quartz monzonite showing porphyritic texture with plagioclase and alkali feldspar phenocrysts. Mineral abbreviation: Afs, alkali feldspar; Pl, plagioclase; Frct, ferrorichterite; Qtz, quartz; Bt, biotite.

Journal Pre-proof

Fig. 3. Plot of $Al_2O_3/(Na_2O + K_2O)$ versus $Al_2O_3/(CaO + Na_2O + K_2O)$ (all in molar proportion) for the volcanic and plutonic rocks from the Yunshan caldera complex (Maniar and Piccoli, 1989). Data from Yan et al. (2018a).

Fig. 4. SHRIMP zircon $^{206}Pb/^{238}U$ ages (a) and zircon $\varepsilon_{Hf}(t)$ values (b) for the volcanic and plutonic rocks from the Yunshan caldera complex. The weighted mean ages of the samples F374-1, F380-1 and F371-2 were reported using “Tuff Zirc age” of

ISOPLOT (Ludwig, 2001) to extract a “best” age with accepted MSWD. Data from Yan et al. (2018a).

Fig. 5. Cathodoluminescence (CL) images of representative zircon grains, and corresponding trace element concentrations and elemental ratios of the studied samples from the Yunshan caldera complex.

Fig. 6. Trace element compositional variations in zircons from the Yunshan caldera complex. Hollow rhombus and solid rhombus denote zircon cores and CL-bright rims and whole grains, respectively. Data of zircons from the Turkey Creek caldera (Deering et al., 2016) and Yandangshan caldera complex (Yan et al., 2018b) are shown for comparison. (d) Rayleigh fractional crystallization modeling results. Model 1 (grey line) is calculated using a fractional crystallization assemblage of K-feldspar (35%), plagioclase (30%), clinopyroxene (10%), amphibole (20%), biotite (5%), and accessory zircon (0.01%). Model 2 (black line) is calculated using a fractional crystallization assemblage of K-feldspar (15%) + plagioclase (55%) + clinopyroxene (15%) + amphibole (5%) + magnetite (10%). The starting composition for Model 1 is the least evolved zircon composition of mafic microgranular enclave (F371-1-15). The starting compositions for Model 2 is the calculated average zircon composition of the most evolved zircon composition from the peraluminous rhyolite and the least evolved zircon composition from mafic microgranular enclave. The partition coefficients of all phases used in this model are listed in Supplementary Table 3.

Journal Pre-proof

Fig. 7. Whole-rock trace element compositional variations of the volcanic and plutonic rocks from the Yunshan caldera complex. (a) Rb versus Sr. (b) Eu/Eu* versus Sr. Data from Yan et al. (2018a).

Fig. 8. Schematic model illustrating the generation of magmas of the peraluminous rhyolites and peralkaline rhyolites from the Yunshan caldera complex. The peraluminous rhyolitic melts were initially extracted from a silicic mush (a). The silicic mush was rejuvenated by mafic magma recharge after the extraction of peraluminous rhyolitic melt and then underwent plagioclase dominated fractionation, resulting in a peralkaline composition of the extracted melt (b). The extracted peraluminous and peralkaline rhyolitic magmas would be assembled and stored in melt lens within the mush zone before eruptions.

Journal Pre-proof

Declaration of competing interests

☒ The authors declare that they have no known competing financial interests or personal relationships that could have appeared to influence the work reported in this paper.

☐The authors declare the following financial interests/personal relationships which may be considered as potential competing interests:

Journal Pre-proof

Highlights

- Volcanic-plutonic link was revealed by zircon trace elements from caldera complex;
- Peralkaline rhyolite extracted from rejuvenated mush after peraluminous rhyolite extraction;
- Contrasting compositions of volcanic and plutonic zircons imply crystal–melt segregation;
- Multistage zircon crystallization reflects magma recharge processes.

Journal Pre-proof

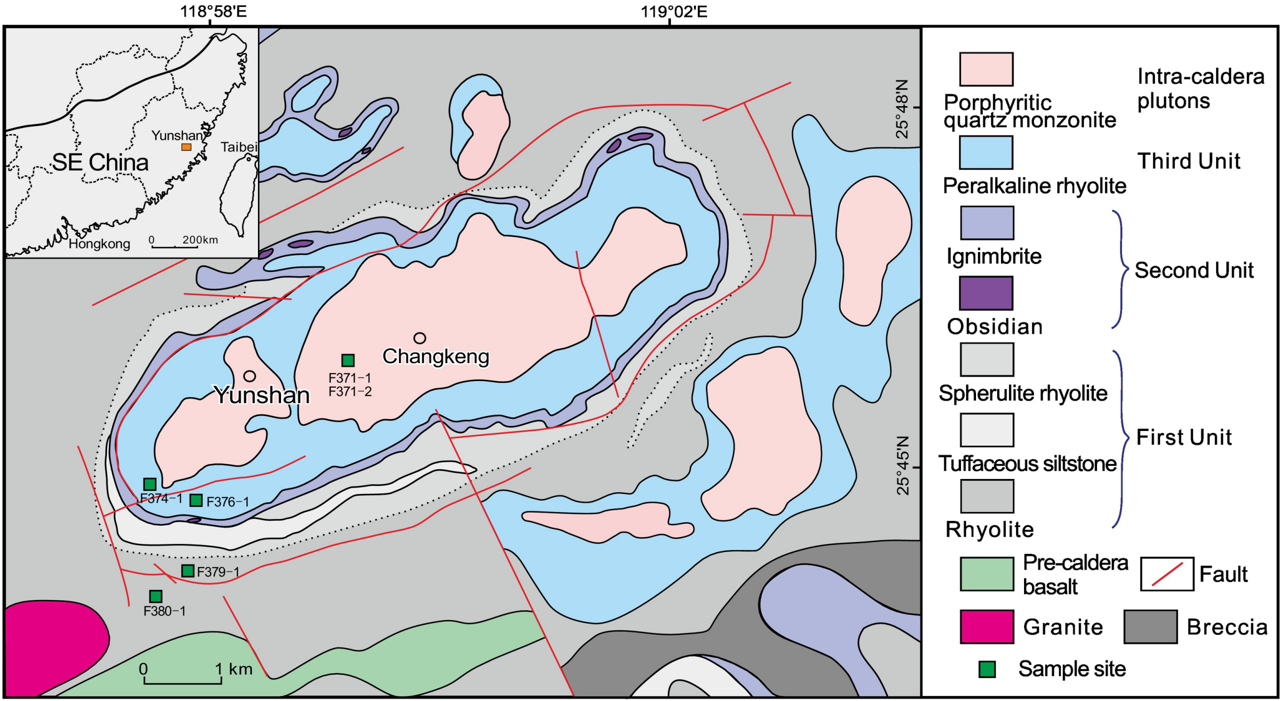
118°58'E
119°02'E
25°48'N
25°45'N
Yunshan
Taibei
SE China
Hongkong
0 200km
Changkeng
Yunshan
F371−1
F371−2
F374−1
F376−1
F379−1
F380−1
0 1 km
Porphyritic quartz monzonite
Intra-caldera plutons
Peralkaline rhyolite
Third Unit
Ignimbrite
Obsidian
Second Unit
Spherulite rhyolite
Tuffaceous siltstone
Rhyolite
First Unit
Pre-caldera basalt
Fault
Granite
Breccia
Sample site

Figure 1

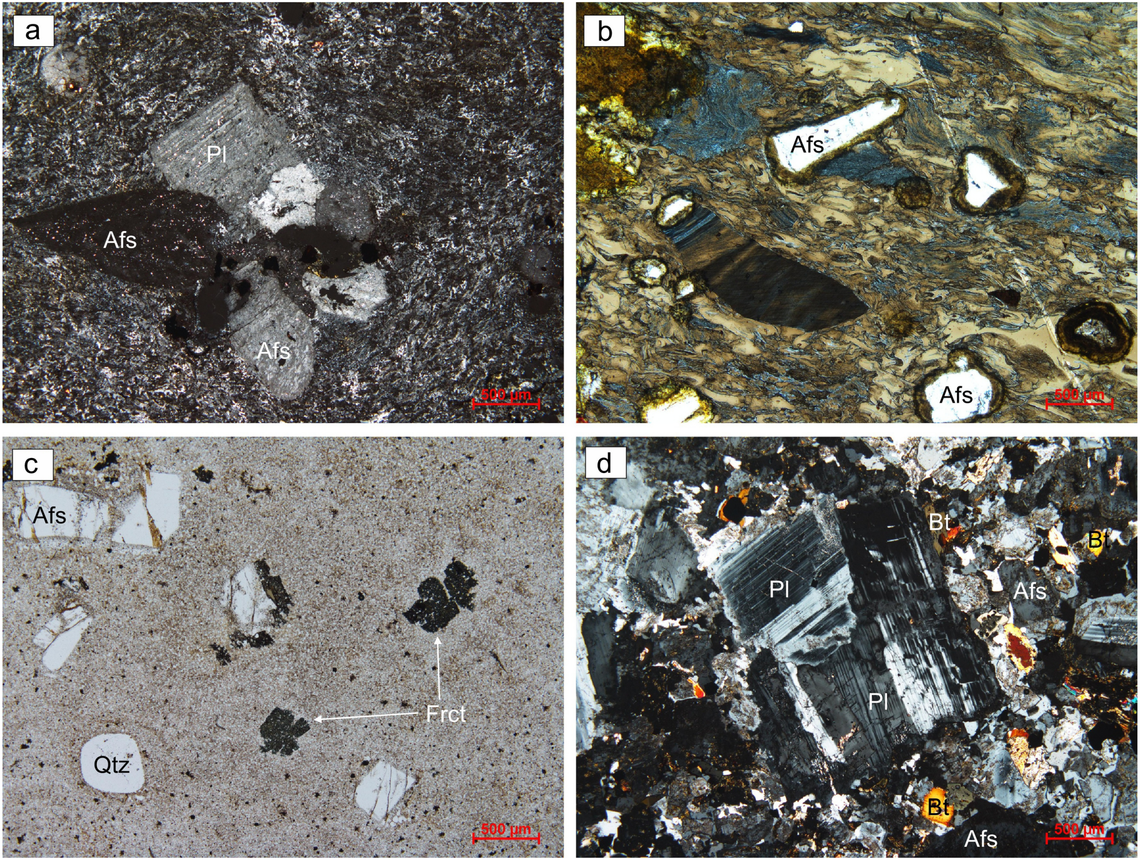
a
Pl
Afs
Afs
500 µm
b
Afs
Afs
500 µm
c
Afs
Qtz
Frct
500 µm
d
Bt
Bt
Pl
Afs
Pl
Bt
Afs
500 µm

Figure 2

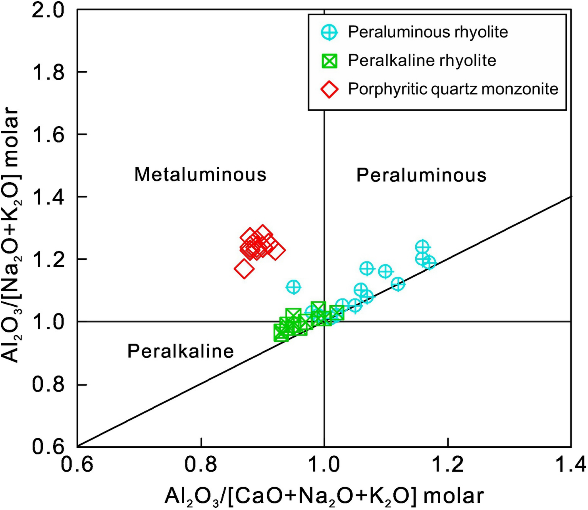

2.0
1.8
1.6
1.4
1.2
1.0
0.8
0.6
0.6
0.8
1.0
1.2
1.4
$Al_2O_3/[Na_2O+K_2O]$ molar
$Al_2O_3/[CaO+Na_2O+K_2O]$ molar
Peraluminous rhyolite
Peralkaline rhyolite
Porphyritic quartz monzonite
Metaluminous
Peraluminous
Peralkaline

Figure 3

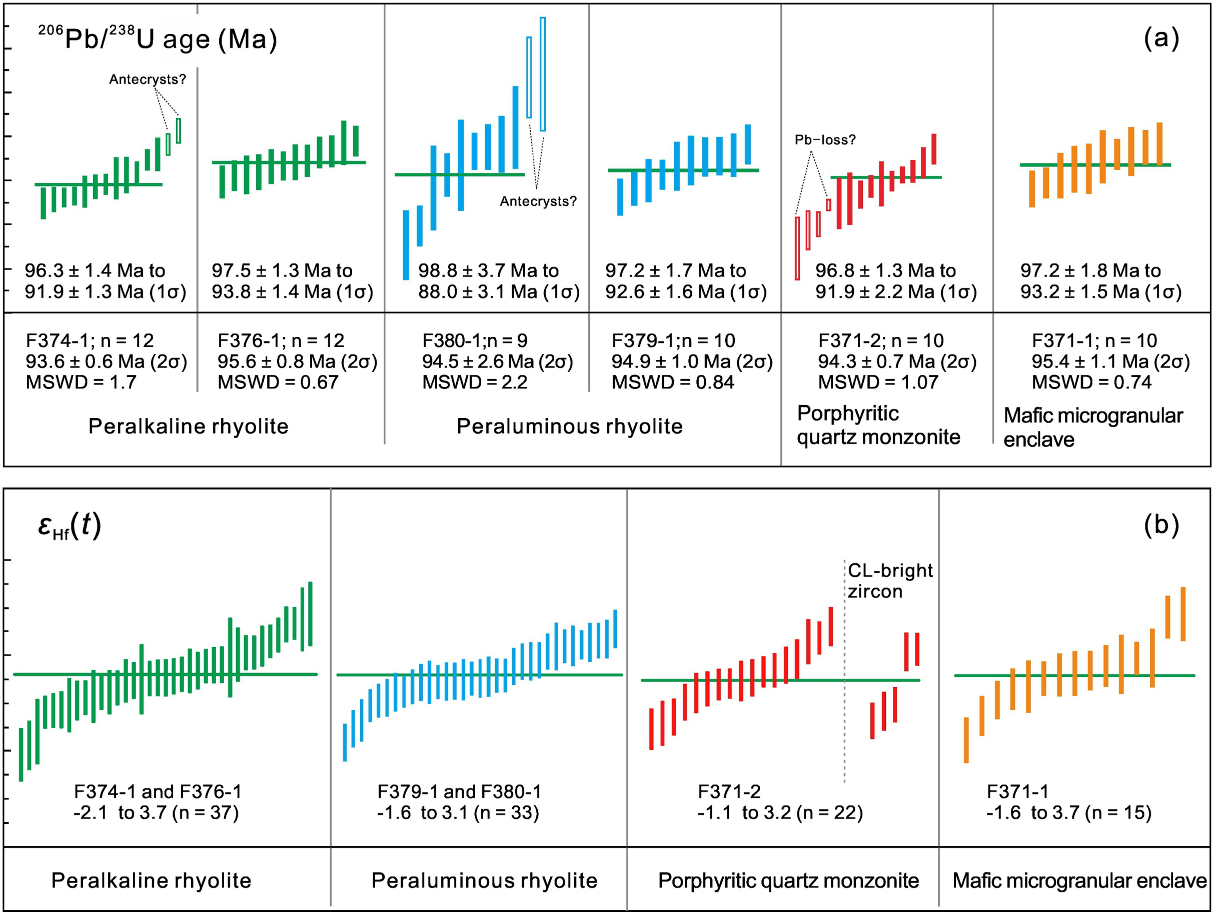
^{206}Pb/^{238}U age (Ma)
(a)
106
102
98
94
90
86
82
Antecrysts?
Antecrysts?
Pb−loss?
96.3 ± 1.4 Ma to 91.9 ± 1.3 Ma (1σ)
97.5 ± 1.3 Ma to 93.8 ± 1.4 Ma (1σ)
98.8 ± 3.7 Ma to 88.0 ± 3.1 Ma (1σ)
97.2 ± 1.7 Ma to 92.6 ± 1.6 Ma (1σ)
96.8 ± 1.3 Ma to 91.9 ± 2.2 Ma (1σ)
97.2 ± 1.8 Ma to 93.2 ± 1.5 Ma (1σ)
F374-1; n = 12 93.6 ± 0.6 Ma (2σ) MSWD = 1.7
F376-1; n = 12 95.6 ± 0.8 Ma (2σ) MSWD = 0.67
F380-1;n = 9 94.5 ± 2.6 Ma (2σ) MSWD = 2.2
F379-1;n = 10 94.9 ± 1.0 Ma (2σ) MSWD = 0.84
F371-2; n = 10 94.3 ± 0.7 Ma (2σ) MSWD = 1.07
F371-1; n = 10 95.4 ± 1.1 Ma (2σ) MSWD = 0.74
Peralkaline rhyolite
Peraluminous rhyolite
Porphyritic quartz monzonite
Mafic microgranular enclave
εHf(t)
(b)
6
2
-2
-6
CL-bright zircon
F374-1 and F376-1 -2.1 to 3.7 (n = 37)
F379-1 and F380-1 -1.6 to 3.1 (n = 33)
F371-2 -1.1 to 3.2 (n = 22)
F371-1 -1.6 to 3.7 (n = 15)
Peralkaline rhyolite
Peraluminous rhyolite
Porphyritic quartz monzonite
Mafic microgranular enclave

Figure 4

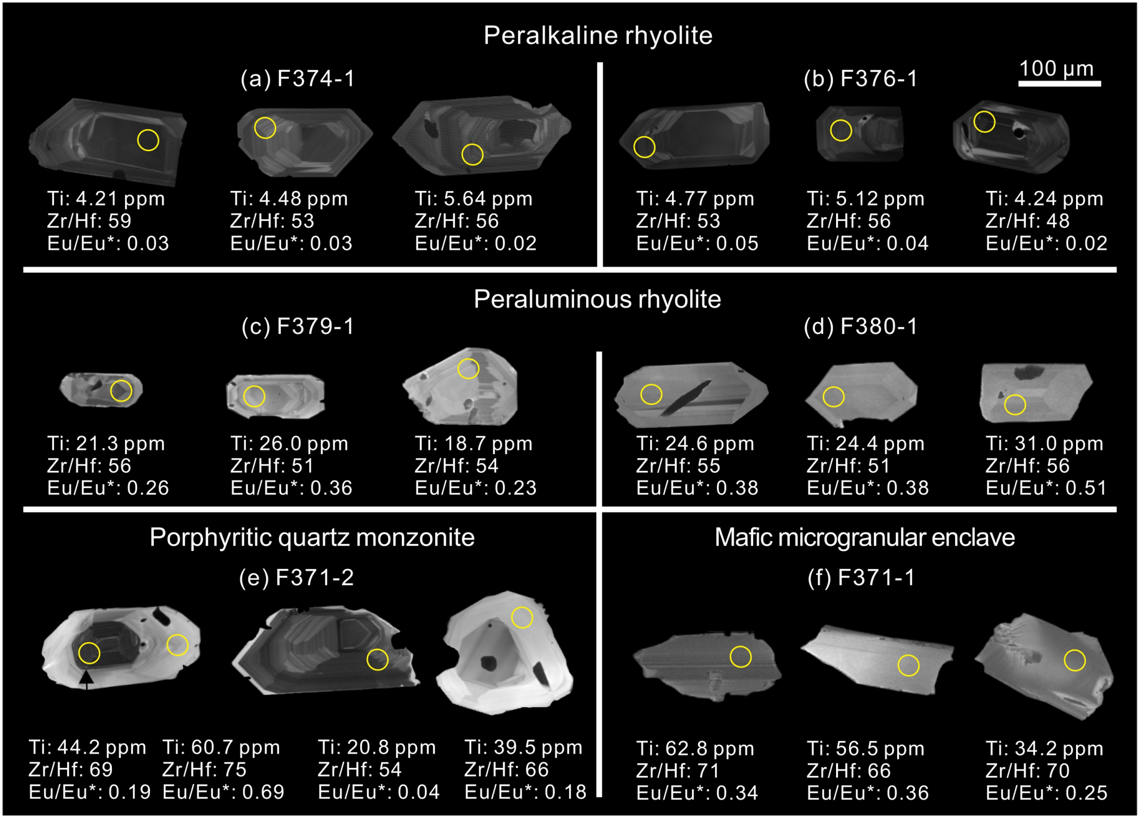
Peralkaline rhyolite
(a) F374-1
Ti: 4.21 ppm
Zr/Hf: 59
Eu/Eu*: 0.03
Ti: 4.48 ppm
Zr/Hf: 53
Eu/Eu*: 0.03
Ti: 5.64 ppm
Zr/Hf: 56
Eu/Eu*: 0.02
(b) F376-1
100 μm
Ti: 4.77 ppm
Zr/Hf: 53
Eu/Eu*: 0.05
Ti: 5.12 ppm
Zr/Hf: 56
Eu/Eu*: 0.04
Ti: 4.24 ppm
Zr/Hf: 48
Eu/Eu*: 0.02
Peraluminous rhyolite
(c) F379-1
Ti: 21.3 ppm
Zr/Hf: 56
Eu/Eu*: 0.26
Ti: 26.0 ppm
Zr/Hf: 51
Eu/Eu*: 0.36
Ti: 18.7 ppm
Zr/Hf: 54
Eu/Eu*: 0.23
(d) F380-1
Ti: 24.6 ppm
Zr/Hf: 55
Eu/Eu*: 0.38
Ti: 24.4 ppm
Zr/Hf: 51
Eu/Eu*: 0.38
Ti: 31.0 ppm
Zr/Hf: 56
Eu/Eu*: 0.51
Porphyritic quartz monzonite
(e) F371-2
Ti: 44.2 ppm
Zr/Hf: 69
Eu/Eu*: 0.19
Ti: 60.7 ppm
Zr/Hf: 75
Eu/Eu*: 0.69
Ti: 20.8 ppm
Zr/Hf: 54
Eu/Eu*: 0.04
Ti: 39.5 ppm
Zr/Hf: 66
Eu/Eu*: 0.18
Mafic microgranular enclave
(f) F371-1
Ti: 62.8 ppm
Zr/Hf: 71
Eu/Eu*: 0.34
Ti: 56.5 ppm
Zr/Hf: 66
Eu/Eu*: 0.36
Ti: 34.2 ppm
Zr/Hf: 70
Eu/Eu*: 0.25

Figure 5

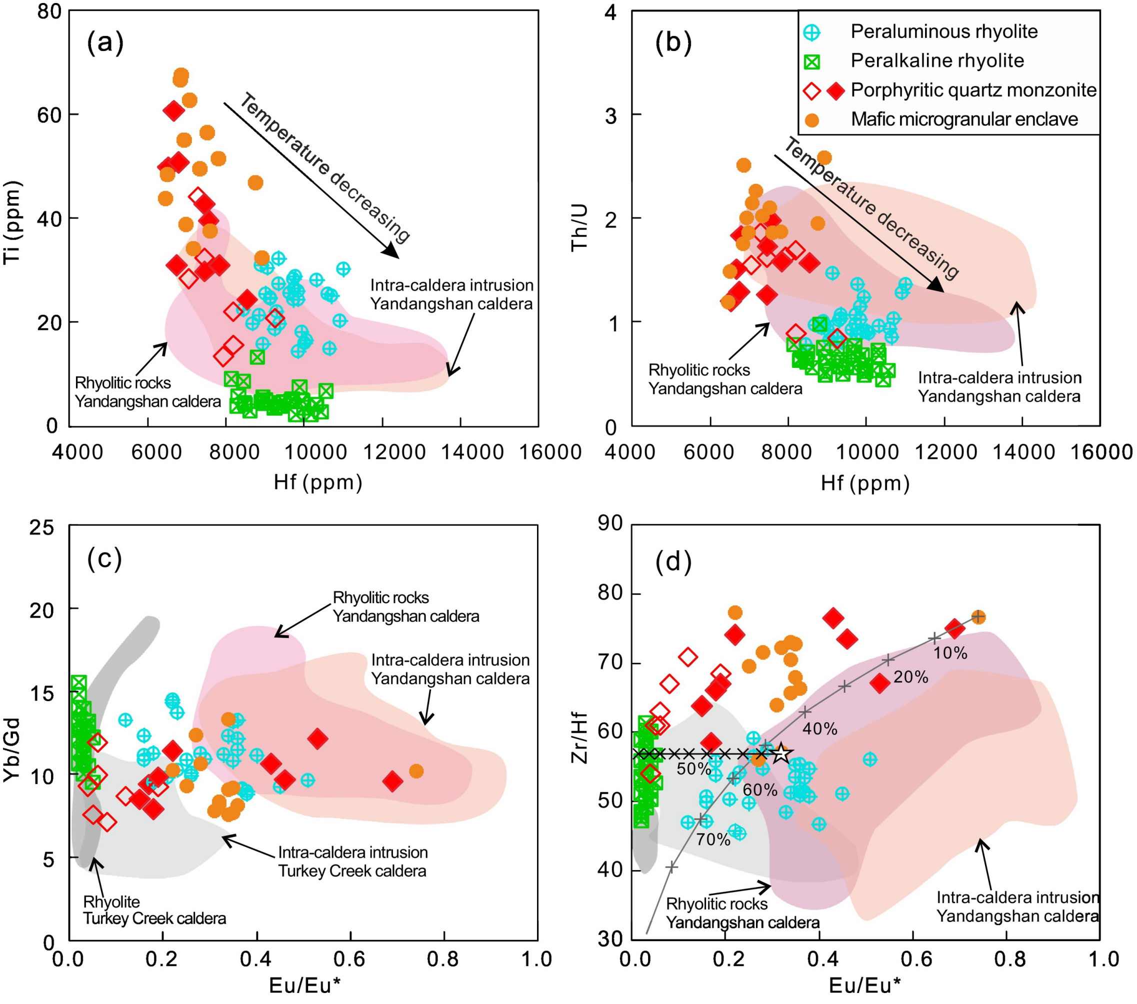
(a)
Ti (ppm)
Hf (ppm)
Temperature decreasing
Intra-caldera intrusion Yandangshan caldera
Rhyolitic rocks Yandangshan caldera
(b)
Th/U
Hf (ppm)
Peraluminous rhyolite
Peralkaline rhyolite
Porphyritic quartz monzonite
Mafic microgranular enclave
Temperature decreasing
Rhyolitic rocks Yandangshan caldera
Intra-caldera intrusion Yandangshan caldera
(c)
Yb/Gd
Eu/Eu*
Rhyolitic rocks Yandangshan caldera
Intra-caldera intrusion Yandangshan caldera
Intra-caldera intrusion Turkey Creek caldera
Rhyolite Turkey Creek caldera
(d)
Zr/Hf
Eu/Eu*
10%
20%
40%
50%
60%
70%
Rhyolitic rocks Yandangshan caldera
Intra-caldera intrusion Yandangshan caldera

Figure 6

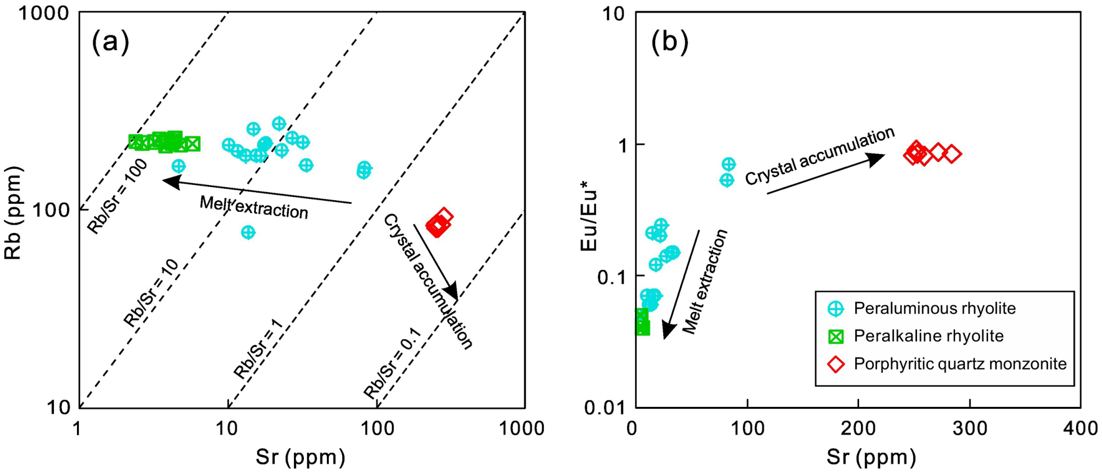
(a)
Rb (ppm)
Sr (ppm)
1000
100
10
1
10
100
1000
Rb/Sr = 100
Rb/Sr = 10
Rb/Sr = 1
Rb/Sr = 0.1
Melt extraction
Crystal accumulation
(b)
Eu/Eu*
Sr (ppm)
10
1
0.1
0.01
0
100
200
300
400
Crystal accumulation
Melt extraction
Peraluminous rhyolite
Peralkaline rhyolite
Porphyritic quartz monzonite

Figure 7

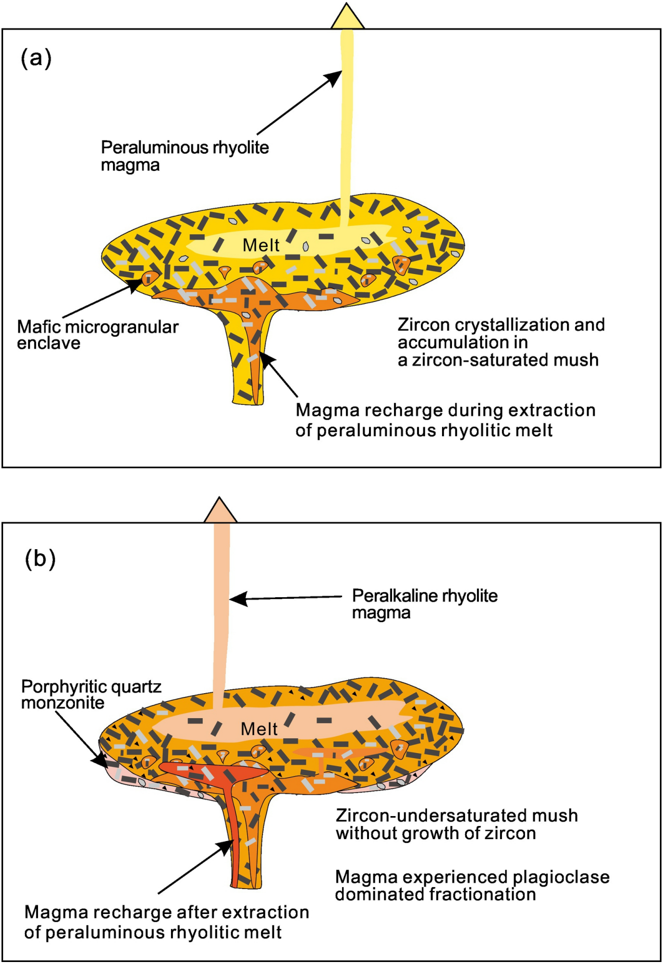
(a)
Peraluminous rhyolite magma
Melt
Mafic microgranular enclave
Zircon crystallization and accumulation in a zircon-saturated mush
Magma recharge during extraction of peraluminous rhyolitic melt
(b)
Peralkaline rhyolite magma
Porphyritic quartz monzonite
Melt
Zircon-undersaturated mush without growth of zircon
Magma experienced plagioclase dominated fractionation
Magma recharge after extraction of peraluminous rhyolitic melt

Figure 8